



High-aperture EUV microscope using multilayer mirrors and a 3D reconstruction algorithm based on z-tomography

I. V. MALYSHEV,^{1,*}  D. G. REUNOV,¹ N. I. CHKHALO,¹
M. N. TOROPOV,¹  A. E. PESTOV,¹  V. N. POLKOVNIKOV,¹
N. N. TSYBIN,¹ A. YA. LOPATIN,¹ A. K. CHERNYSHEV,¹
M. S. MIKHAILENKO,¹ R. M. SMERTIN,¹  R. S. PLESHKOV,¹
AND O. M. SHIROKOVA²

¹Institute for the Physics of Microstructures of the Russian Academy of Science, 7 Academicheskaya Str., Nizhny Novgorod, Russia

²Federal State Budgetary Educational Institution of Higher Education “PIMU” of the Ministry of Health of Russia, Nizhny Novgorod, Russia

*ilya-malyshev@ipmras.ru

Abstract: The article is devoted to the development of an EUV microscope using a wavelength of 13.84 nm. Due to the use of a mirror lens with a large numerical aperture, $NA = 0.27$, and a short depth of focus, it has been possible to carry out z-tomography of bio-samples for the first time with this type of microscope. A 3D image was reconstructed, and a pixel resolution of 140 nm was obtained. A new simple algorithm for the 3D reconstruction of absorption images from z-tomography data has been proposed that takes into account lens aberrations and a point spread function. The algorithm reduces the inverse absorption task to the corresponding well-studied task of fluorescence microscopy, with an error of 10% for cells up to 10 μm thick.

© 2022 Optica Publishing Group under the terms of the [Optica Open Access Publishing Agreement](#)

1. Introduction

For a detailed study of cells in biology and medicine, it is necessary to obtain their images with nanometer resolution [1]. Optical microscopy operating in visible light does not allow direct examination of the nanostructure of living cells with details less than 200 nm due to diffraction blurring [2]. Various methods for increasing the resolution of optical microscopy, such as STED microscopy [3], have made it possible to significantly exceed the diffraction limit and to achieve resolutions in the order of tens of nanometers. However, as in the case of classical fluorescence microscopy, the method allows one to see only stained organelles in isolation from the environment, which makes it difficult to understand the processes occurring in the cells.

Electron microscopy can provide a high, spatial resolution in the order of nanometers [4]. However, to conduct such studies, the samples have to be frozen and cut into films with a thickness of 100–500 nm, i.e. this method is destructive and cannot be used to study living cells [5]. Atomic force and scanning tunneling microscopy make it possible to study only the surfaces of samples.

On the other hand, soft X-ray microscopy (SXR) has been developing for more than 30 years in the spectral region of the “water transparency window”, at wavelengths of 2.3–4.4 nm [6–10], as well as in the EUV region at wavelengths of 13.4–13.8 nm [11–15]. The main advantages of this method in the “water window” are:

- the diffraction limits of the short wavelengths provides for spatial resolutions in nanometers;

- natural: the order-of-magnitude (or better) contrast between the absorption by carbon-containing structures and water makes it possible to study samples without the use of contrasting and/or fluorescent substances;
- relatively high transmission and practically no scattering of radiation enables the study of cells and tissue sections up to 10–15 μm thick in their native, potentially, living state;
- sample preparation is significantly simplified in comparison with existing nanoscopy methods.

At present, 3D images of frozen cells up to 10–15 μm thick with a volume resolution of up to 60 nm (according to the Fourier-Shell period criterion) have been obtained when using synchrotron sources [6–8] and of up to 100 nm with laboratory laser-plasma sources [9,10].

Microscopes in the EUV range are also being actively developed. They are used to obtain 2D images of dried cells, as well as masks for EUV lithographs [11,12]. For example, in [13], an image of a silicon cell of *Chrisodidymus* was obtained with a lateral resolution of about 50 nm. In [14], images of CT26 fibroblast cells and of algal diatoms were obtained with lateral resolutions of about 100 nm. In [15], the structure of a section of mouse brain was studied.

The lateral resolution of microscopes in the “water transparency window” can reach 10 nm [16,17], while the volume resolution, as shown above, is several times poorer. The main factor limiting the 3D resolution in SXRМ when using Fresnel zone plates is the large depth of focus, which forces the use of technically complex angular tomography to reconstruct the bulk structure of the samples. The limited number of angular projections together with decentering of the sample during angular scanning also affect the 3D resolution [10].

The use of normal-incidence multilayer X-ray mirrors instead of Fresnel zone plates makes it possible to increase the numerical aperture of the projection objectives. In this case, the area of localization of the region sharply observed by the lens along its optical axis, defined depth of focus (DOF), can be reduced by an order of magnitude, and for a numerical aperture $\text{NA} = 0.3$ and wavelength $\lambda = 3$ nm it will be

$$\text{DOF} = \lambda/\text{NA}^2 = 33 \text{ nm} \quad (1)$$

From a practical point of view, this means that the largest contribution to the image formed on the detector will be made by a region of the sample with a thickness of ± 33 nm. Therefore, as in the case of confocal microscopy, one can switch from angular to z-tomography and reconstruct a three-dimensional structure from a series of projections taken when the sample is shifted along the optical axis of the microscope [18]. In this case, the lateral resolution for incoherent illumination δx will be

$$\delta x = 0.61 \cdot \lambda/\text{NA} = 6 \text{ nm} \quad (2)$$

which is still substantially better than the longitudinal resolution. However, this problem of z-tomography can be further solved by shooting an additional z-stack for a sample rotated at two or three different angles.

The main obstacle to the development of high-aperture soft X-ray microscopy based on multilayer, normal-incidence mirrors is the extremely high requirements for the smoothness and shape accuracy of the mirror substrates. According to the Marechal criterion, to ensure the diffraction quality of the images, the root mean square (RMS) error of aberrations of the projection lens should not exceed $\lambda/14$. In the “water window” this corresponds to about 0.2 nm. As our calculations and practice show, by taking into account the point spread function reconstructed from the measured lens aberrations, the required diffraction quality of the image can also be obtained with aberrations of $\lambda/8$ – $\lambda/4$, i.e. up to 0.4–0.8 nm.

At present, primarily due to the development of EUV lithography, there has been significant progress in the technology of manufacturing high-precision mirrors; in particular, the ZEISS

company has achieved substrate manufacturing accuracy at the level of $\text{RMS} = 0.1 \text{ nm}$ [19]. The results obtained by the authors of this work are inferior to these results and are at a level of $\text{RMS} = 0.6\text{--}0.8 \text{ nm}$ [20,21], which is, however, already sufficient to create a high-resolution lens. The methods that have been developed for fabricating and characterizing high-precision substrates are described in [22].

The aims of our work were to develop a high-aperture microscope based on a two-mirror Schwarzschild lens, and a mathematical model that allows for three-dimensional reconstruction of the structure of samples using the z-tomography technique. This algorithm can be used for both EUV and “water window” microscopy. In conclusion, a demonstration of the resulting methods is given using examples of imaging biosamples of a dried section of a lily of the valley (*convallaria*) and a section of mouse brain cells at a wavelength of $\lambda = 13.84 \text{ nm}$.

2. EUV microscope

2.1. Installation description

The scheme and a photograph of the microscope are shown in Fig. 1. The laser-plasma source (LPS) consists of an “Ekspla Nd:YAG NL 303” laser ($\lambda = 1064 \text{ nm}$, $E_{\text{pulse}} = 0.5 \text{ J}$, duration 5 ns , frequency 10 Hz), whose radiation is focused on an argon gas target (pos. 1 in Fig. 1). The pulsed gas target was constructed using an electromagnetic valve as described in [23]. The maximum gas pressure at the valve inlet, under which it works stably, was 3 atm . We used the bright line of the ArVIII ion at a wavelength of $\lambda = 13.84 \text{ nm}$.

An Mo/Si mirror (pos. 2) collects LPS radiation (pos. 1) on a sample installed in the subject area of the objective (pos. 3). The collector has the shape of an ellipsoid. After aspherization and local shape correction, its focusing spot from a point source was measured and had an FWHM size of $20 \mu\text{m}$ [24], which makes it possible to collect the source radiation from the sample effectively. The maximum drop in sample illumination intensity in the field of view of $290 \times 290 \mu\text{m}^2$ was 10% (maximum in the center, minimum at the edges). The holder with the sample is mounted on a piezoceramic slider, which provides for z-tomography by moving along the optical axis. The image of the sample with a magnification of 46 times is built with a two-mirror objective (pos. 4) on a CMOS detector with a pixel count of 2048×2048 and a pixel size of $6.5 \mu\text{m}$ (pos. 6). The aspherical concave mirror of the lens provides a large aberration-free field of view with a size of $290 \times 290 \mu\text{m}^2$. After the lens, a Mo/ZrSi₂ filter (pos. 5) is installed, which suppresses long-wavelength radiation but transmits at 13.84 nm [25].

The procedure for image search and sharpening was as follows. The Mo/ZrSi₂ filter on the motorized slide was extended to adjust the position of the sample in visible light from a photodiode temporarily placed at the bottom focus of the elliptical mirror. Then the installation was pumped out, and the image of the sample was viewed, illuminated by the laser plasma. If the filter is pulled out, then an image can be seen in visible light, if pushed in, then at 13.84 nm .

A “Standa” optical pneumatic table (pos. 7) is used to isolate the microscope optics from vibration. A stand with the optics (pos. 8) is supported by springs (pos. 9) and rests in contact with three rubber supports (pos. 10) installed under it. The stand is held on top by holders that prevent it from swinging (pos. 11). So that the holders do not transmit vibrations, there are rubber gaskets between them and the stand. A soft bellows (pos. 12) and rubber plates between the pump frame and the table legs were used to decouple the turbomolecular pump from the vacuum chamber.

The projection lens body is made of invar with a low thermal expansion coefficient. For passive stabilization of the temperature changes in the distance between the lens mirrors, heat compensators made of materials with different thermal expansion coefficients were used.

To reduce noise within the detector, it was provided with cooling. To do this, a radiator was installed under the matrix, which, using 30 copper wires 30 cm long and 1 mm in diameter, was connected to a copper finger cooled from the outside with nitrogen vapor to $-80 \text{ }^\circ\text{C}$ (pos. 3 in

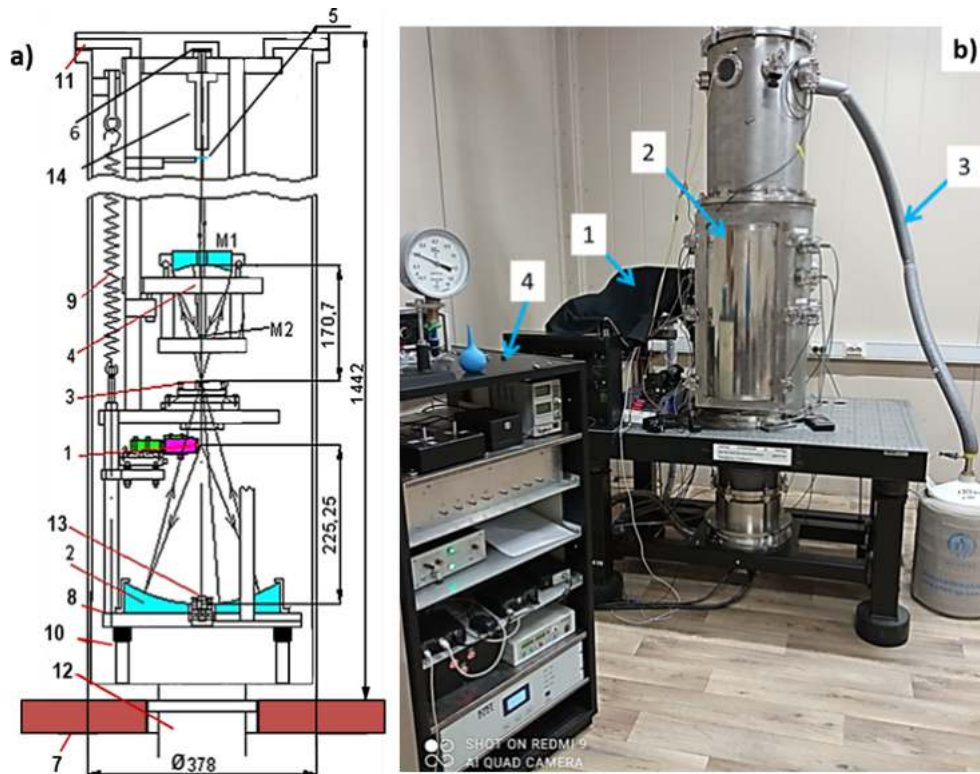


Fig. 1. a) Scheme of the EUV mirror microscope: 1) laser-plasma source based on a pulsed gas target and an IR laser, 2) a multilayer elliptical collector mirror, 3) the sample under study on a 5D table with the possibility of z-scanning in vacuum, 4) two-mirror lens — 46x with a field of view of $290 \times 290 \mu\text{m}^2$ and an aspherical mirror M1, 5) filter for suppressing long-wavelength radiation, 6) X-ray CMOS backlight matrix detector “GPixel Gsense 2020 BSI Pulsar”, 7) “Standa” optical table, 8) stand for the optics, 9) springs, 10) supports with rubber inserts, 11) holders for stand, 12) bellows for turbomolecular pump, 13) alignment laser, 14) blind. b) Photograph of the EUV microscope: 1) IR laser under the mantle, 2) vacuum chamber with optics, 3) detector cooling system, 4) stand with the microscope’s electronic control systems.

Fig. 1(b)). When operating without the cooling system, the matrix detector heated up to 43 °C. The temperature rose no higher, because the heat had time to escape to the metal case of the detector and then to the massive stand. When the cooling system was turned on, the detector temperature did not rise above 23 °C. This cooling was sufficient, because the detector starts to become noisy only if its temperature is above 36 °C.

Since vibrations can adversely affect the resolution of a microscope, much attention was paid to addressing their measuring. To do this, instead of an X-ray detector, a special magnification optics system (24×) was installed. The optics system is described in more detail in [26]. With this, the total magnification was 1100 ×. Given a pixel size of 6.5 μm, this corresponds to a pixel resolution in the object plane of 6 nm. A fiber-optic source of a reference spherical wave with a size of 0.25 μm [27] was installed in the object plane, and the position of its enlarged image was recorded over time. The measurements showed that the vibrations of the image, reduced to the object plane, were at a “Peak to Valley” of 6 nm (PV) during daily working hours, and much less than 6 nm at night.

An X-ray CMOS matrix detector with a quantum detection efficiency of about 95% in the 13 nm region was used for the experiments described [28]. For a magnification of 46 times and a pixel size of 6.5 μm, the size of its projection on the plane of the sample was 140 nm.

2.2. Projection lens

The most important element of the microscope, which determines its resolving power, is the projection lens. The Schwarzschild scheme was used for the projection lens. Table 1 shows its parameters. The concave mirror M1 is aspherical, the convex mirror M2 is spherical. The mirror was aspherized according to the method in [29] using a wide ion beam ($d = 100$ mm) through a metal mask, made on an electro-erosion machine with numerical control. The shape of the aspherical mirror is described by the polynomial:

$$z(r = 0 : 50) = \frac{(1/137) \cdot r^2}{1 + \sqrt{1 - (1/137)^2 \cdot r^2}} + \alpha_2 \cdot r^2 + \alpha_4 \cdot r^4 + \alpha_6 \cdot r^6 + \alpha_8 \cdot r^8 + \alpha_{10} \cdot r^{10}, \quad (3)$$

where $\alpha_2 = -1.919 \cdot 10^{-6}$, $\alpha_4 = 7.3144 \cdot 10^{-10}$, $\alpha_6 = 3.9214 \cdot 10^{-14}$, $\alpha_8 = 1.7221 \cdot 10^{-18}$, $\alpha_{10} = -1.4635 \cdot 10^{-22}$.

Table 1. Schwarzschild lens parameters 46×

	Distance to the next element, mm	Curvature radius, mm	Size, mm
Field of view on a sample	170.7		$\approx 0.29 \times 0.29 \text{ mm}^2$
Mirror M1	102.5	137	$\varnothing 100$
Mirror M2	812.4	-24	$\varnothing 10$
Image on detector	-		$13.3 \times 13.3 \text{ mm}^2$, pixel $6.5 \times 6.5 \text{ } \mu\text{m}^2$

The resolution of a microscope is determined by errors in the shape of its objective mirrors. Aberrations were measured in a point diffraction interferometer operating in the phase recording mode. The lens aberrations were corrected on the M1 mirror using an ion beam with a minimum diameter of 2 mm, using the setup as in [29]. After the final correction of the shape of M1, an interferogram was obtained and measured (Fig. 2(a)). The obtained aberrations of the projection lens had RMS = 2.6 nm (Fig. 2(b)), i.e. better than $\lambda/5$. More details about the measurements of roughness, shape, ion-beam correction and aspherization of the shape of substrates, as well as a deposition of multilayer reflective coatings can be found in [24].

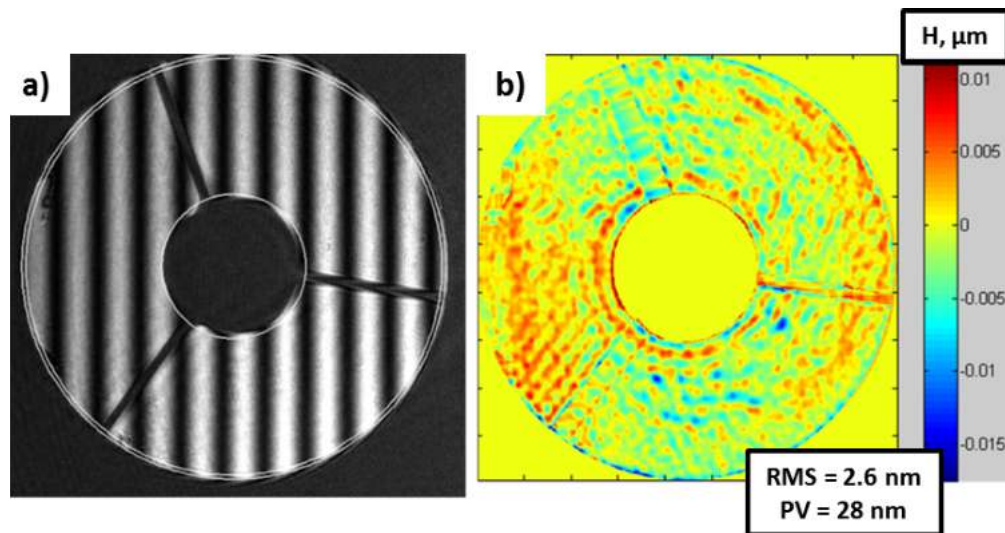


Fig. 2. After final shape corrections and deposition of the reflective multilayer coatings on the mirrors: a) interferogram; b) lens aberrations (measurements were carried out in a point diffraction interferometer [30]).

After correcting the lens aberrations, multilayer Mo/Si reflective coatings were deposited by magnetron sputtering. The internal stress in the films was minimized in order to reduce the distortion could introduce. The reflection coefficient of the mirrors was about 60% in the vicinity of $\lambda = 13.84$ nm, Fig. 3.

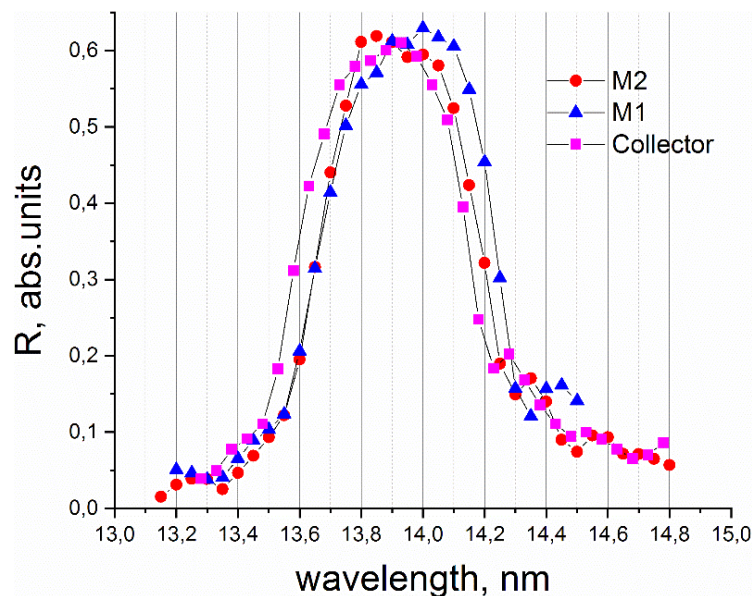


Fig. 3. Measured spectral dependences of the reflection coefficient of the Mo/Si coating of the objective mirrors.

After installing the projection lens in the microscope, the aberrations worsened a little, up to an $RMS = \lambda/4$. Perhaps this was due to the induced deformation when the projection lens

was installed in the microscope. Based on the measured aberrations, a three-dimensional point spread function h (PSF) was generated in the ZEMAX, Fig. 4. The caustic diameter was 140 nm ($\approx 80\%$ energy), and was equal to one pixel of the detector matrix projected into the object space. The axial length of the caustic was about 0.8 μm , which is close to the diffraction limit equal to $4\text{DOF} = 4\lambda/\text{NA}^2 = 0.76 \mu\text{m}$ ($\lambda = 13.84 \text{ nm}$, $\text{NA} = 0.27$) [31], and almost 2 times shorter than it for high-aperture confocal microscope ($L_{\text{caustic}} = 4n\lambda/\text{NA}^2 = 1.44 \mu\text{m}$, where $n = 1.51$ (oil-immersion), $\lambda = 470_{\text{HM}}$, $\text{NA} = 1.4$) [2].

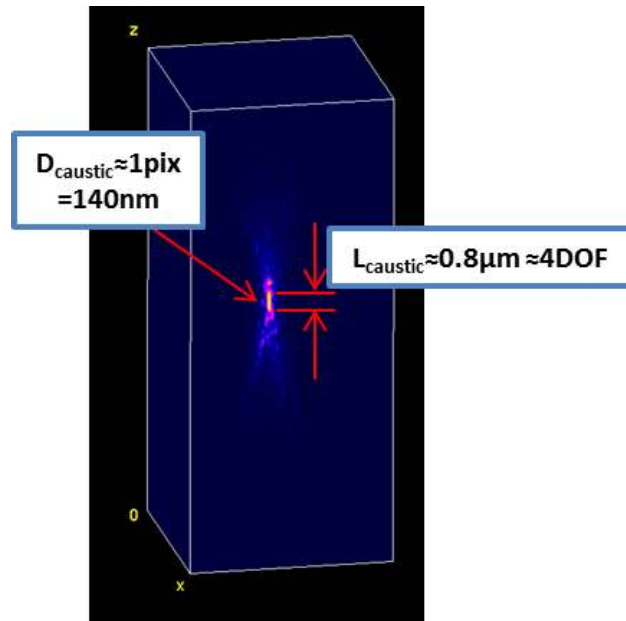


Fig. 4. Point spread function (PSF) of the EUV microscope generated from the measured aberrations and taking into account diffraction ($\lambda = 13.84 \text{ nm}$, $\text{NA} = 0.27$).

3. Algorithm for the reconstruction of 3D images in high-aperture SXR microscopy based on z-tomography data

3.1. Imaging model in high-aperture SXR microscopy

Consider an imaging model in a high-aperture SXR microscope based on general principles. In Fig. 5, a collector creates uniform illumination of all points in the sample, including in the focal z -plane (indicated by the dotted line on Fig. 5). A divergent cone beam emerges from each of its points, with a numerical aperture $\text{NA}_{\text{illumination}} = 0.3$ greater than the aperture of the projection lens $\text{NA}_{\text{lens}} = 0.27$. Partial coherence factor $= \text{NA}_{\text{illumination}}/\text{NA}_{\text{lens}} > 1$, so the illumination is incoherent, according to [32]. The projection mirror lens makes an image of the focal z -plane on the matrix detector.

The image of point 1, located inside the cell, is projected by the lens at point 1' (Fig. 5). As we move towards point 1 and away from it, the intensity of each ray I_0 decreases due to the absorption in the cell, which is characterized by the absorption coefficient μ , this being a function of the coordinates. Experimentally, the input intensity I_0 can be obtained by removing the sample. We will assume that it does not depend on the xy -coordinates, if this is not the case, then the images can always be normalized:

$$I_0^{\text{norm}} = \max(I_0(x, y)), \quad (4)$$

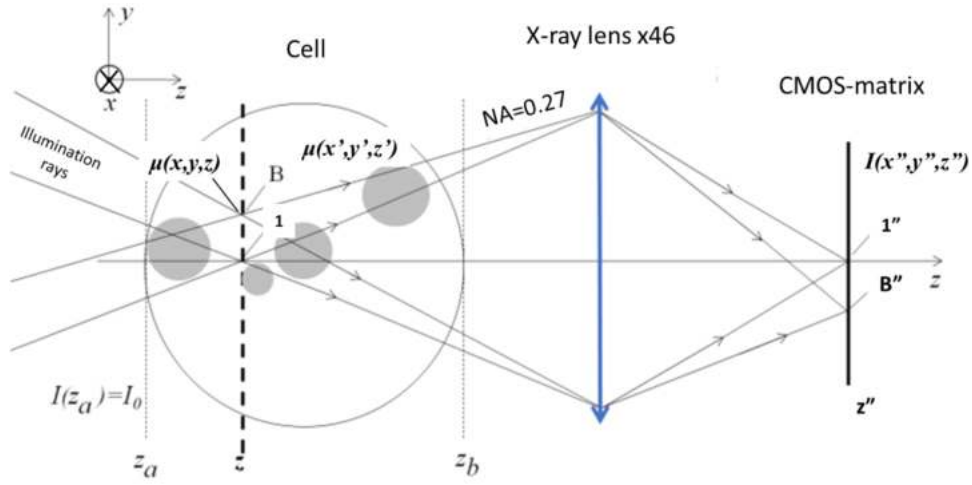


Fig. 5. Image formation in absorption contrast, in a high-aperture SXR microscope.

$$I_{norm}(x, y) = \frac{\max(I_0)}{I_0(x, y)} \cdot I(x, y). \quad (4a)$$

I_0^{norm} does not depend on the coordinates after this normalization, so we will denote it below simply by I_0 , so as not to overload the formulas.

If there was one ray, then for incoherent radiation the intensity in the image space would be described according to the Beer-Lambert law:

$$I(x'', y'', z'') = I_0 \cdot \exp\left(- \int_{L_{ray}} \mu(x + x', y + y', z + z') dl'\right) \quad (5)$$

where x'', y'' are the coordinates of point $1''$ on the camera, which are related to the coordinates of the point (x, y) and the lens magnification G , according to the law: $x'' = Gx, y'' = Gy$ ($G < -1$, since a two-mirror lens without internal focus flips and enlarges the image). There is no z'' coordinate on the recording matrix, in fact, z'' is the z -number of the image on the matrix during z -tomography of the sample, because by shifting the sample along z , we sharply image its different z -sections. dl' is an elementary ray segment codirectional with it. L_{ray} is the length of the ray over the entire thickness of the cell. Coordinates x', y', z' are “running” and take both positive and negative values, and change along the ray. The absorption coefficient μ describes the three-dimensional structure of the cell.

Because there are many rays, then the intensity of each point in the image space is described by a formula, where the arithmetic average over all rays is taken:

$$I(x'', y'', z'') = \frac{I_0}{N_{rays}} \sum_{rays} \exp\left(- \int_{L_{ray}} \mu(x + x', y + y', z + z') dl'\right). \quad (6)$$

Since, after integration over the coordinates of the rays x', y', z' only the dependence on x, y, z remains, the left side of (6) can be written as $I(x, y, z)$ instead of $I(x'', y'', z'')$ for simplification the perception of the formula.

$\frac{I_0}{N_{rays}} \sum_{rays}$ means, that for each point (x, y, z) the arithmetic mean inside the light cone is taken from the integrals calculated along each ray, and all these rays intersect at the depicted point (x, y, z) . Coordinates x', y', z' are “running” coordinates of points inside the light cone, counted

from its center. The x', y', z' -coordinate system is centered at the imaged point (x, y, z) . In the Cartesian coordinate system $dl' = dz' / \cos(\alpha')$, where α' is the angle between the z -axis and the ray.

Thus, the inverse problem of the high-aperture soft X-ray microscope (6) is to restore the integrand function of the absorption coefficient $\mu(x, y, z)$ describing the three-dimensional structure of the sample.

Finding the absorption coefficient μ from Eq. (6) is significantly complicated by the fact that the summation over the rays is performed after taking the exponential. However, in the low absorption approximation, $\int_{L_{ray}} \mu dl' \ll 1$, ray summation \sum_{rays} be inserted inside the exponent, and then Eq. (6) can be written in the following form:

$$I(x, y, z) = I_0 \exp\left(-\frac{1}{N_{rays}} \sum_{rays} \int_{L_{ray}} \mu(x + x', y + y', z + z') dl'\right) \quad (7)$$

Let us prove the possibility of reducing (6) to (7) if the sample has a small integral absorption. In this case, on the one hand, the right side of (6) can be simplified by expanding the exponent in a series:

$$\frac{I_0}{N_{rays}} \sum_{ray} \exp\left(-\int_{L_{ray}} \mu dl'\right) \approx \frac{I_0}{N_{rays}} \sum_{rays} \left(1 - \int_{L_{ray}} \mu dl'\right) = \frac{I_0}{N_{rays}} \left(N_{rays} - \sum_{rays} \int_{L_{ray}} \mu dl'\right) \quad (8)$$

On the other hand, the right-hand side of (7) can also be expanded into a Taylor series $\frac{1}{N_{rays}} \sum_{rays} \int_{L_{ray}} \mu dl' \ll 1$ under the condition, which obviously follows from $\int_{L_{ray}} \mu dl' \ll 1$

$$I_0 \exp\left(-\frac{1}{N_{rays}} \sum_{rays} \int_{L_{ray}} \mu dl'\right) \approx I_0 \left(1 - \frac{1}{N_{rays}} \sum_{rays} \int_{L_{ray}} \mu dl'\right) = \frac{I_0}{N_{rays}} \left(N_{rays} - \sum_{rays} \int_{L_{ray}} \mu dl'\right) \quad (9)$$

Since the right parts of equalities (8) and (9) are equal, their left parts are also equal:

$$\frac{I_0}{N_{rays}} \sum_{rays} \exp\left(-\int_{L_{ray}} \mu dl'\right) \approx I_0 \exp\left(-\frac{1}{N_{rays}} \sum_{rays} \int_{L_{ray}} \mu dl'\right) \quad (10)$$

Thus, we have obtained that, in the case of a small integral absorption coefficient the summation over the rays can be inserted inside the exponent and from the complex Eq. (6) the simplified Eq. (7) is obtained.

Let us estimate what errors the expansion of the exponent in a series to a linear term will lead to when studying real samples. Thus, we can determine the area of applicability of this approximation. For example, for the case $\int_{L_{ray}} \mu dl' \ll 1$, transmission is $\exp(-0.4) \approx 0.67$, and within the linear approximation is 0.6, so the error in determining the absorption is about 10% and can be considered acceptable.

Let us consider how the approximate formula (7) works in the case of a model cell at a microscope wavelength of 3.37 nm. To speed up the calculation, we shall define a two-dimensional cell. The cell diameter is 10 μm , the water content is 90%, and protein is 10% (Fig. 6). The average μ over the entire model cell is $0.46 \mu\text{m}^{-1}$, which approximately corresponds to the range of measurement $\mu = 0.2\text{--}0.7 \mu\text{m}^{-1}$ for various organelles [8,33,34].

Figure 7 shows the result of applying formulas (6) and (7) to a model cell. For ease of perception, these images are shown on a logarithmic scale. The RMS deviation of the difference

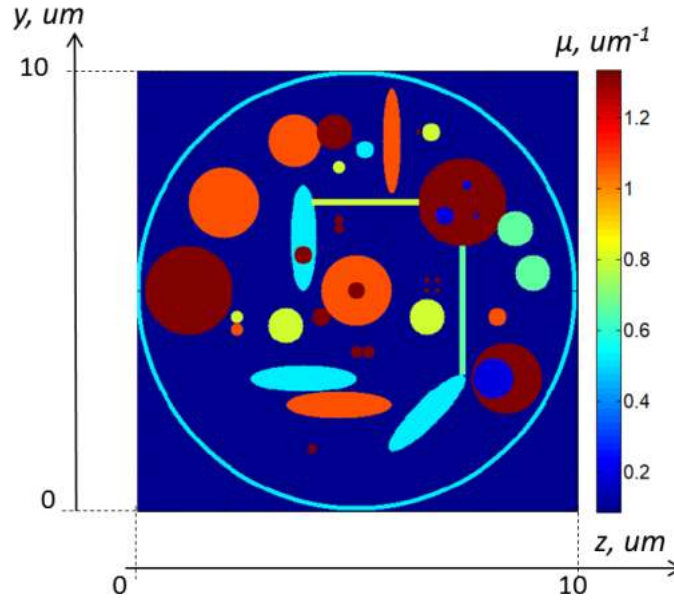


Fig. 6. A 10 μm model cell with a membrane, intracellular substance and organelles of various shapes. The cell is 90% water and 10% protein.

for calculations (6) and (7) is 10% (Fig. 7(c)). Thus, it is numerically shown that with a 10% error, it is possible to use a simplified imaging model (7) in a high-aperture SXR microscopy.

3.2. Transformation of the inverse problem of X-ray absorption microscopy to the classical problem of confocal fluorescence microscopy

To process the images obtained on the detector, in order to restore the three-dimensional distribution of μ in the sample, deconvolution methods should be used that take into account the specific type of experimentally measured PSF. Therefore, let us show that the integration over the rays inside the double light cone, which is inside the exponent in (7), is equal to the convolution with the PSF h , which has the shape of the same double cone. Let us start with a discrete cell model, and then move on to a continuous model. Let, for ease of understanding, the cell has only two “points” (two elementary volumes) with non-zero absorption coefficients μ_1 and μ_2 . In this case, “point” 1 is located exactly in the object plane of the lens, and “point” 2 is at a distance $\Delta z'$ from it and is located inside the light cone of rays emerging from “point” 1 (Fig. 8). Then, passing through “point” 1 (elementary volume 1), each beam will weaken by $\Delta I = I_0(1 - \exp(-\mu_1 \Delta l))$, where Δl is the length of the elementary volume. After point 1, the rays diverge, so not all rays will come to point 2, but only their part, equal to:

$$N \cdot \rho_{\text{rays in p.2}} = \frac{N \cdot \Delta S_d}{S_{\text{beam section}}} = \frac{N \cdot \Delta S_d}{\pi(\Delta z' \cdot \text{tg}(\alpha))^2}, \quad (11)$$

where N is the number of rays passing through “point” 1, ΔS_d is the surface area of the elementary volume that is crossed by the rays at “point” 2, $\rho_{\text{rays in p.2}}$ is the portion of the rays arriving at “point” 2, and $\Delta z'$ is the z -distance between “points” 1 and 2. Each ray passing through “point” 2 will weaken by $\Delta I = I_0(1 - \exp(-\mu_2 \Delta l))$, and, all together, the rays will weaken to:

$$\Delta I_{\Sigma} = N \cdot \rho_{\text{rays in p.2}} \cdot \Delta I = N \cdot \frac{\Delta S_d}{\pi(\Delta z' \cdot \text{tg}(\alpha))^2} \cdot \Delta I = \text{const} \cdot \frac{\Delta I}{\Delta z'^2} \quad (12)$$

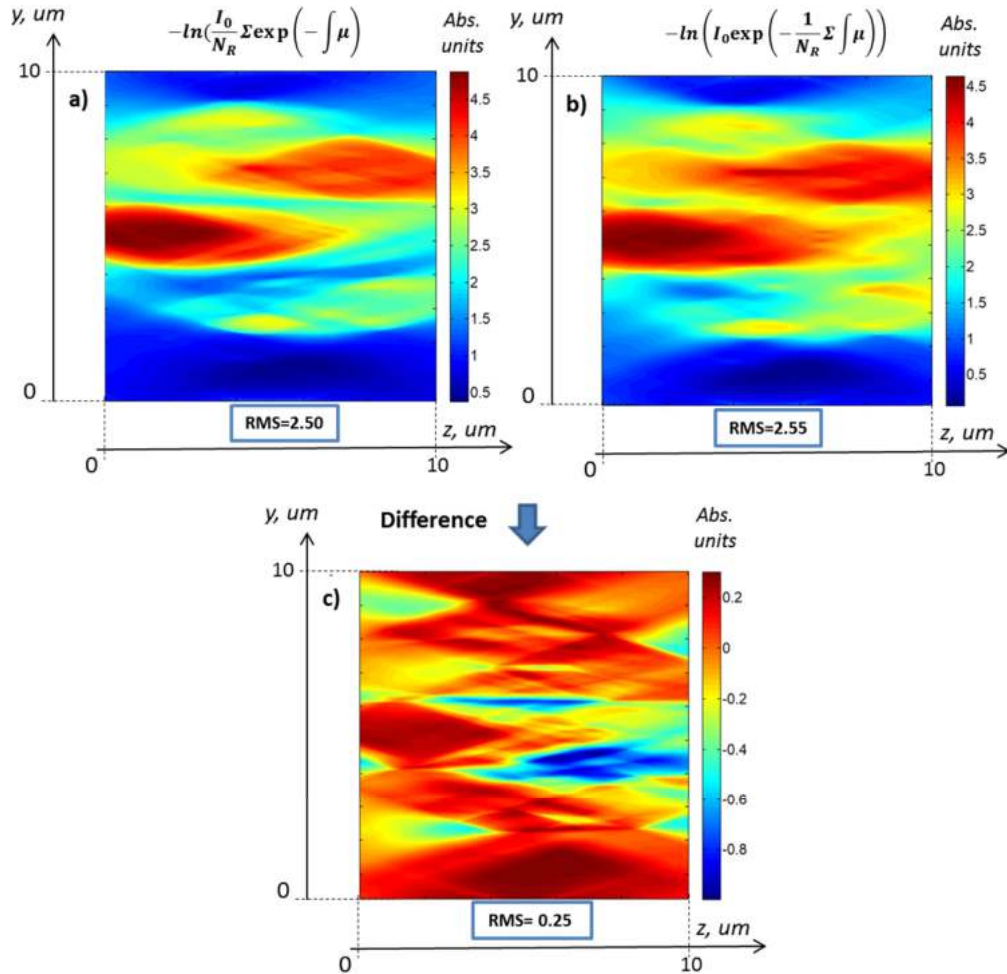


Fig. 7. The result of applying formulas (6) and (7) to the model cell: a) calculation by strict formula (6); b) calculation by approximate formula (7); c) their difference. The z -axis is the optical axis of the microscope, the y -axis lies in a plane parallel to the plane of the detector.

It follows from (12) that the contribution from “point” 2 to the image 1” depends on the square of the distance $\Delta z'$ between the points.

On the other hand, $\Delta l \rightarrow 0$ and $\mu_2 \neq 0$, therefore, the exponent is expanded into a series up to the 1st term:

$$\Delta I = I_0(1 - \exp(-\mu_2 \Delta l)) \approx I_0 \mu_2 \Delta l \tag{13}$$

Substituting (13) into (12), we get that, due to the passage of rays through the point μ_2 , the intensity at “point” 2 will weaken in accordance with the expression:

$$\Delta I_{\Sigma} = N \cdot \rho_{\text{rays in } p.2} \cdot I_0 \mu_2 \Delta l = N \cdot \frac{\Delta S_d}{\pi(\Delta z' \cdot \text{tg}(\alpha))^2} \cdot I_0 \mu_2 \Delta l = \text{const} \cdot \frac{\mu_2}{\Delta z'^2} \tag{14}$$

“Point” 1 and “point” 2 are in the path of the same ray, so they both affect image 1”. Therefore, the intensity of the image of “point” 1 is affected not only by μ_1 , but also by μ_2 with a weighting coefficient dependent on the square of the z -distance between “points” 1 and 2. But this is

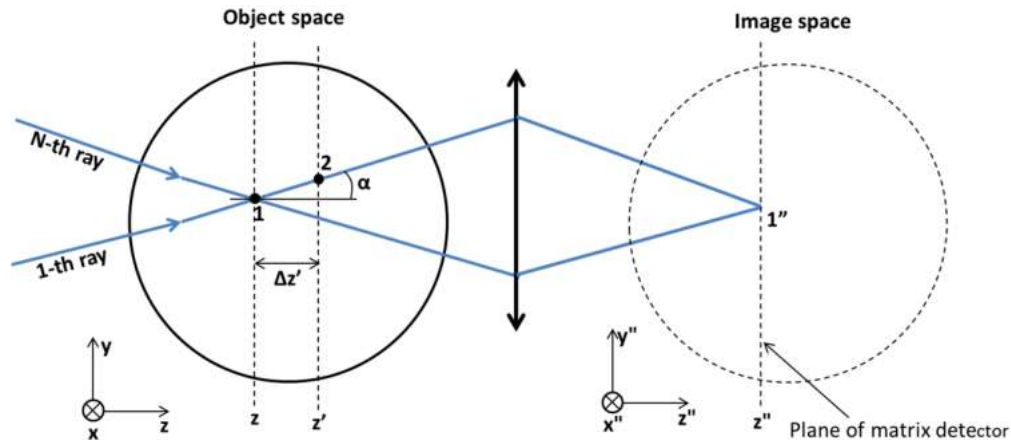


Fig. 8. Relationship between the object space and image space. The angle α is given by the numerical aperture of the projection lens $\alpha = \arcsin(\text{NA})$. “Points” 1 and 2 have nonzero μ .

equivalent to μ_2 is blurred over the volume of the sample by the cone point spread function (PSF) $h(\Delta z') = \frac{\Delta S_d}{S_{\text{beam section}}} = \frac{\Delta S_d}{\pi(\Delta z' \cdot \text{tg}(\alpha))^2} \sim \frac{1}{\Delta z'^2}$ (see Fig. 8).

Any “point” with an area $\Delta S_d = \Delta x_j \Delta y_i$, located inside the circumference of the intersection of the light cone and any z -plane remote from the focal plane by a distance Δz_k , contributes to the image of “point” 1 in the form $(\Delta x_d \Delta y_d) / \pi(\Delta z_k \cdot \text{tg}(\alpha))^2$ (Fig. 9). Therefore, in the image space at “point” 1”, conjugated with the real “point” 1 of the focal plane of the object, instead of μ_1 , we will have an integer sum of contributions from all the “points” located inside the considered out-of-focus z -slice of the cone, and having the corresponding weighting coefficients:

$$\mu'' = \mu_1 + \sum_{j=1}^{N_j} \sum_{i=1}^{N_i} \frac{\Delta x_d \Delta y_d}{\pi(\Delta z_k \cdot \text{tg}(\alpha))^2} \mu_{ij} = \mu_1 + \sum_{x_j} \sum_{y_i} \frac{\Delta x_d \Delta y_d}{\pi((z_k - z_1) \cdot \text{tg}(\alpha))^2} \mu_1(x_j, y_i) \tag{15}$$

$x_j^2 + y_i^2 \leq (\Delta z_k \cdot \text{tg}(\alpha))^2$

These considerations are valid for all z -planes of the cone remote from the focal plane at any Δz_k , both to the left and to the right, therefore, after taking into account the contributions of all z -planes, we obtain:

$$\mu''_1 = \mu_1 + \sum_{\substack{z_k = z_a \\ z_k \neq z_1}}^{z_b} \sum_{x_j} \sum_{y_i} \frac{(x_j - x_1)^2 + (y_i - y_1)^2 \leq (\Delta z \cdot \text{tg}(\alpha))^2}{\pi((z_k - z_1) \cdot \text{tg}(\alpha))^2 z_N} h(\Delta z_k) \cdot \mu_1(x_j, y_i, z_k) \tag{16}$$

where $h(\Delta z_k) = \frac{\Delta x_d \Delta y_d}{\pi((z_k - z_1) \cdot \text{tg}(\alpha))^2 z_N}$ it is nothing but a discrete point spread function. Inside the double light cone, the value of h decreases depending on the distance of the slice $(z_k - z_1)^2$ from the center of the cone. Outside the light cone given by the equation $(x_j - x_1)^2 + (y_i - y_1)^2 \leq ((z_k - z_1) \Delta \text{tg}(\alpha))^2$ function h is 0, ($\alpha = \arcsin(\text{NA}_{\text{lens}})$), therefore, h depends not only on Δz_k , but also implicitly on x_j и y_i ; z_N is a number of z -plane contributing to the image. Let us move from the discrete model to a continuous one, replacing x_j, y_i, z_k with x', y', z' , and x_1, y_1, z_1 with x, y, z .

The number of slices z_N is replaced by the z -thickness of the sample ΔL , then:

$$\mu_1''(x, y, z) = \mu_1(x, y, z) + \int_{z_a}^{z_b} \int_{x_a}^{x_b} \int_{y_a}^{y_b} \mu(x', y', z') \cdot h(x' - x, y' - y, z' - z) dy' dx' dz', \quad (17)$$

$z' \neq z$

where $h(z' - z) = \frac{1}{\pi((z' - z) \cdot \text{tg}(\alpha))^2 \Delta \Delta L}$ is a continuous point spread function not equal to 0, inside the light cone given by the equation $(x' - x)^2 + (y' - y)^2 \leq ((z' - z) \cdot \text{tg}(\alpha))^2$, which explicitly depends on $z' - z$ and implicitly on $x' - x$ and $y' - y$, and ΔL is the z -thickness of the sample. Since the function h at $z = z'$ tends to ∞ , then, by the property that the convolution integral with the δ -function is equal to the value of the convolution function, Eq. (17) can be written as:

$$\mu_1''(x, y, z) = \int_{z_a}^{z_b} \int_{x_a}^{x_b} \int_{y_a}^{y_b} \mu(x', y', z') \cdot h(x' - x, y' - y, z' - z) dy' dx' dz' = \mu \otimes h. \quad (18)$$

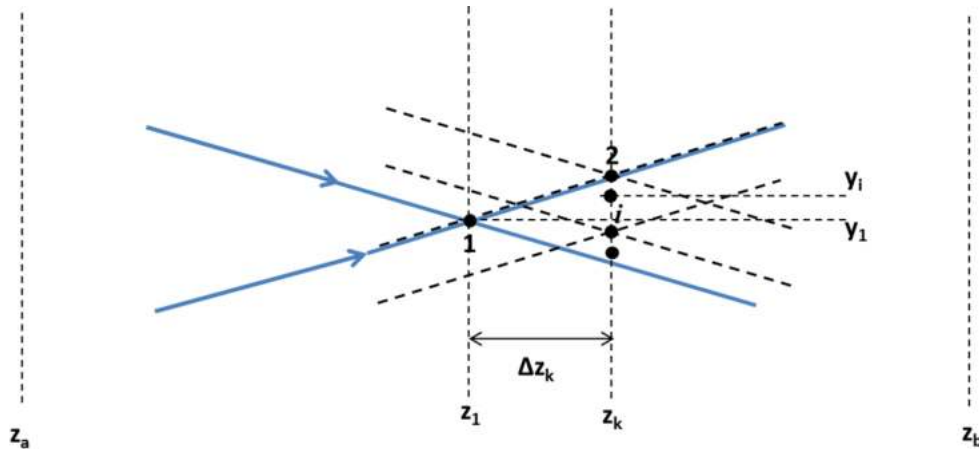


Fig. 9. Image formation of focal “point” 1, explaining the contribution of the points of the light cone plane that are Δz_k away from the focal plane.

There is a complete analogy between Eqs. (16) and (18), because:

1. Coordinates x_j, y_i, z_k changed to x', y', z' ; coordinates x_1, y_1, z_1 changed to x, y, z ; summation $\sum_{z_k} \sum_{x_j} \sum_{y_i}$ changed to $\int \int \int dy' dx' dz'$, where x', y', z' are the “running” coordinates, taking all values within the cell from its beginning z_a to end z_b , from the left edge x_a to the right edge x_b and from the bottom edge y_a to the top edge y_b , by analogy with discrete coordinates z_k, x_j, y_i in Eq. (16).
2. The function value $h(x' - x, y' - y, z' - z)$ under the integral depends on $z' - z$, showing how the “running” point (x', y', z') is distanced from the imaged point (x, y, z) , just as in Eq. (16) h depends on $z_k - z_1$.
3. The values of the function μ are taken in the “running” coordinates (x', y', z') by analogy with the “running” coordinates x_j, y_i, z_k in Eq. (16).

Equation (18) can be written for any point (x, y) of the z -section, because a full-field microscope makes an image of the entire x, y -focal section at once.

Further, as a result of the displacement of the sample along z , each of its z -sections turns up in the focal z -plane of the lens, so law (18) works in turn for each focal z -section, and therefore, for any μ at any point of the sample in the corresponding point of the image, the microscope images a signal not only from μ , but also from neighboring points located inside the double light cone centered at the point μ .

From Eq. (7) we found that in order to obtain an image of some point μ , we need to integrate over all the rays inside the light cone with a vertex at this point (perform the operation $\sum_{\text{rays}} \int_{L_{\text{ray}}} \mu dl'$).

It follows from the above reasoning that such an integration over rays in Eq. (7) is equal to a convolution $\mu \otimes h$, therefore (7) can be written as:

$$I(x, y, z) = I_0 \exp(-\mu \otimes h \cdot \Delta L). \quad (19)$$

We have also verified this numerically. For a cell with a random distribution $\mu(x, y, z)$ as shown in Fig. 6, the numerically-found right side of Eq. (19) exactly coincides with the calculated right side of the previously written Eq. (7) and is approximately equal to the calculated right side of the Beer-Lambert Eq. (6), therefore, according to the z -stack data captured by the microscope $I(x, y, z)$, we can find μ by writing Eq. (19) as:

$$-\ln(I/I_0)/\Delta L = \mu \otimes h. \quad (20)$$

where ΔL is the z -thickness of the cell and is equal to $z_b - z_a$; the right side of Eq. (20) coincides with the right side of the classical inverse problem of fluorescence microscopy [2], and the left side is the minus logarithm of the z -stack of the images $I(x', y', z')$ obtained in a soft X-ray microscope and normalized to the input intensity. Equation (20) is solved by classical deconvolution methods such as the Richardson-Lussy method used for image reconstruction in confocal fluorescence microscopy:

$$\mu = -\ln(I/I_0)/\Delta L \otimes^{-1} h. \quad (21)$$

Note that in Eq. (21), as in Fig. 7, the logarithm of the resulting image I is used, therefore the numerical estimate of the error of this approach is at the level of 10% for cells up to 10 μm thick.

The advantages of the proposed approach are: 1) the possibility of using widely developed methods for solving the inverse problem of confocal fluorescence microscopy and 2) taking into account an experimentally measured PSF of a microscope. We are aware of works on iterative methods for reconstructing images of strongly absorbing samples in confocal fluorescent microscopes [35,36]. The intensity of images of deep sections is mathematically enhanced, which makes it possible to remove the effect of intensity decay in the depth of the sample. However, these methods do not take into account the absorption after the imaged slice, and therefore are not suitable for SXR microscopy.

4. Experimental images, their processing and reconstruction

Images of two objects were obtained using our EUV microscope at a wavelength of 13.84 nm. The first object was a 25 μm thick dried section of the stem of the May lily of the valley (*Convallaria majalis*). Figure 10 shows its image after performing all the procedures: denoising, normalizing the intensity in z -sections, eliminating xy -shift in the z -scan, normalizing to the intensity without a sample, and in the final after logarithm and deconvolution with PSF, according to Eq. (21), in the ImageJ program with the DeconvolutionLab2 plugin [2].

The recovered absorption coefficients μ ranged from 0 to 3 μm^{-1} . The average μ was 1 μm^{-1} . In general, the sample is fairly well reconstructed. Not only the cell walls, but also the

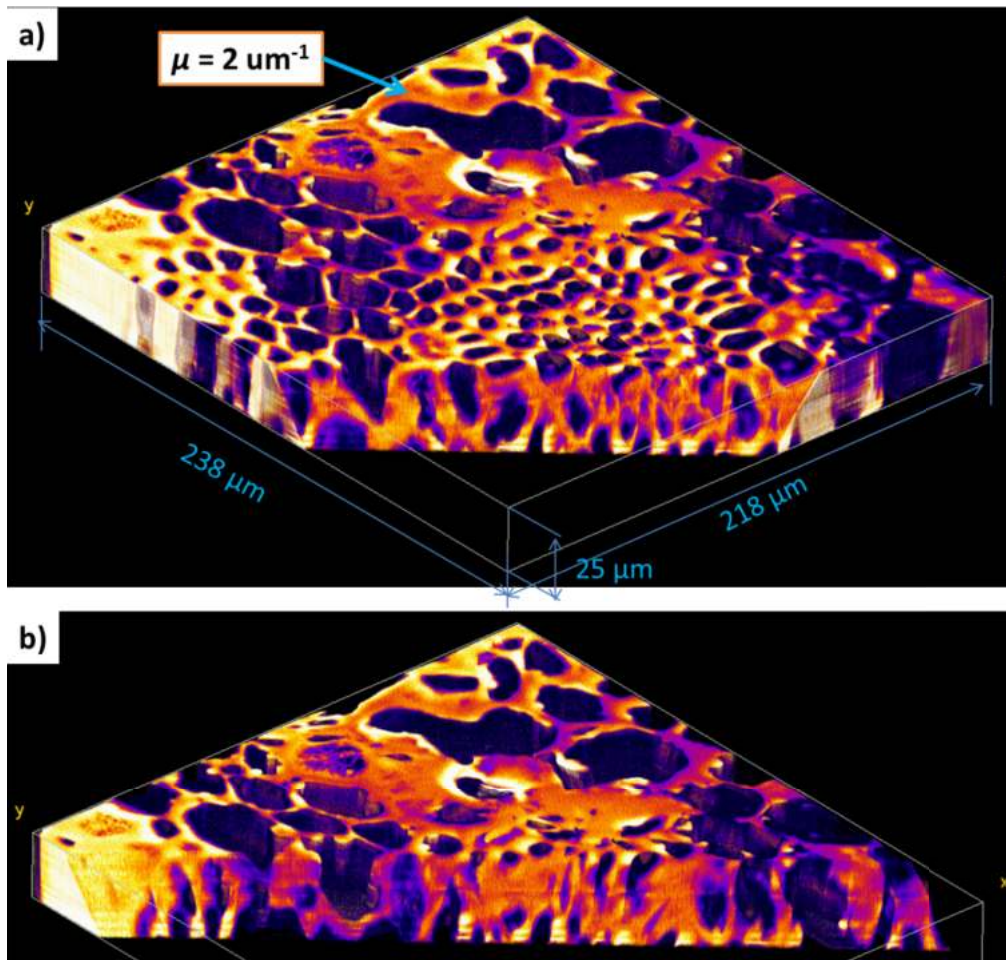


Fig. 10. a), b) — Two sections of the EUV image of a fixed section of convallaria stem, giving an idea of its 3D structure. After preprocessing, logarithm and deconvolution by the Richardson-Lussy method with 400 iterations.

intracellular structures are visible (Fig. 11). The cell cross section (yellow line in Fig. 11) and the cell wall cross section (Fig. 12) show that the lateral resolution is 1 pixel = 140 nm in terms of intensity decay at the level of 20–80%. Since the 25 μm slice of the convallaria lay on the 0.5 mm hole of the object table, having warped slightly, the cells were at different depths, with only a part of the sample being in focus at the same time. When performing the z -scan, we saw that different parts of the sample were in focus.

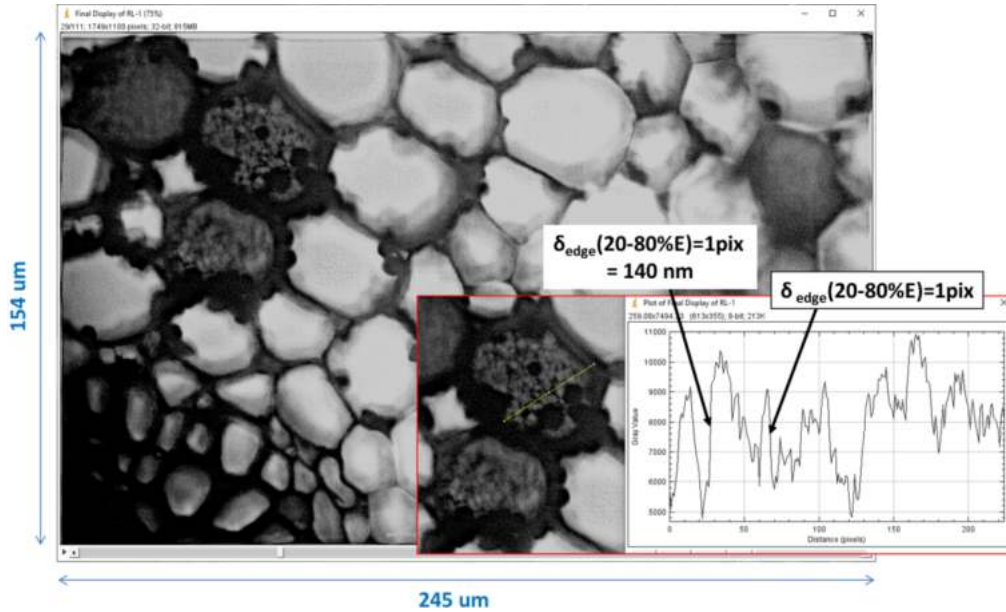


Fig. 11. EUV image of the stem slice of *Convallaria majalis*.

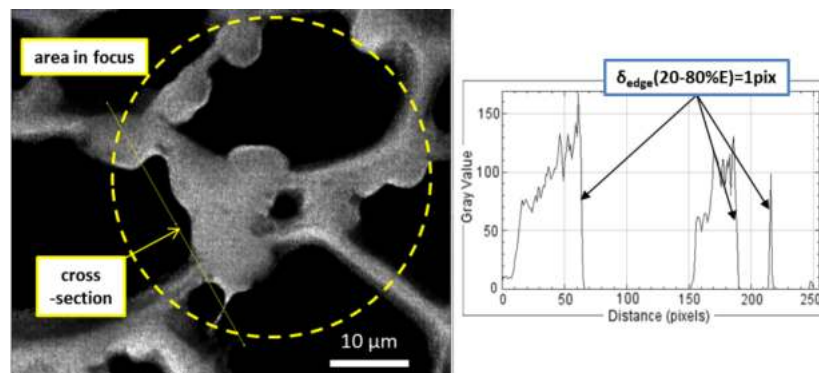


Fig. 12. Cell wall in the focal plane of the lens.

An axial section of the stem slice of *Convallaria majalis* is shown in Fig. 13. The resolution along the axis was up to 0.42 μm , near the half-length of the PSF caustic (see Fig. 4).

Another interesting object was a slice of mouse primary hippocampal cells on the 18th day of development *in vitro*. (Fig. 14). Cell cultures were preliminarily fixed with 2.5% glutaraldehyde and osmium tetroxide, dehydrated in increasing concentrations of ethanol, and embedded in

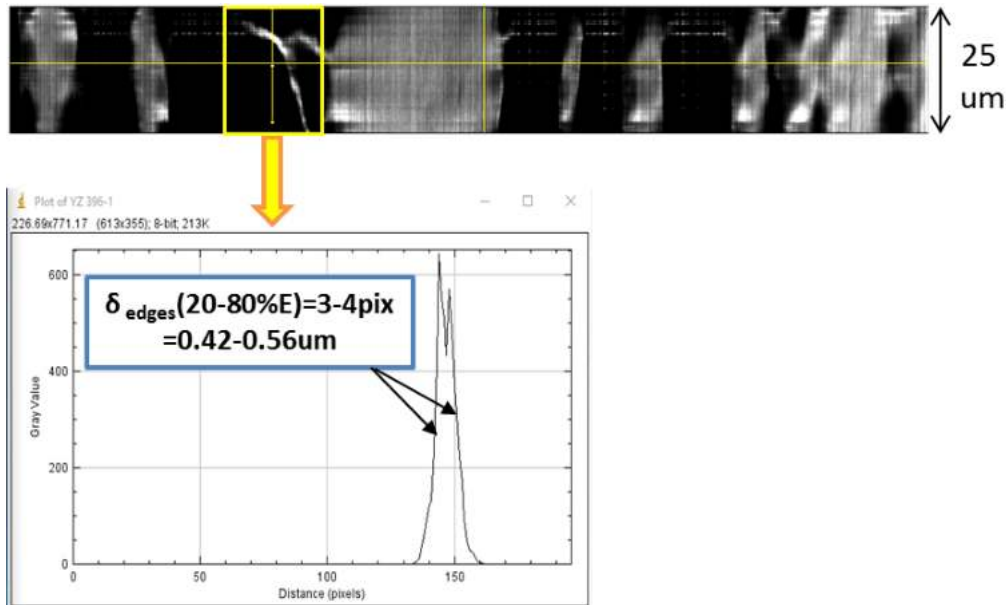


Fig. 13. An axial section the stem slice of *Convallaria majalis*.

Epon 812 resin. After polymerization, the cells were cut on a Leica UC7 ultratome into sections 0.5 μm thick. The sample preparation protocols are given in Appendix 1.

After logarithm and deconvolution by the proposed algorithm the resolution had increased significantly, as can be seen by comparing Figs. 14(a) and 14(b). This made it possible to view the shape of the cell, the cell nucleus, the nucleus/cytoplasm ratio, and the cell matrix. However, it is still insufficient for analysis of the most complex networks of the neuronal processes.

To reconstruct the 3D structure, it is necessary to image slices with a thickness much greater than the length of the PSF-caustic, equal in this case to 0.8 μm . In the EUV range, porous samples would be clearly visible, such as, slices of plant stems, the matrices of some porous but strong connective tissues, and bone tissue would be clearly visible. To obtain three-dimensional images of all types of cells, one needs to go to the “water window”, because the contrast there will be between the carbon-containing matter and the weakly absorbing water, while the frozen water itself act as a fixative.

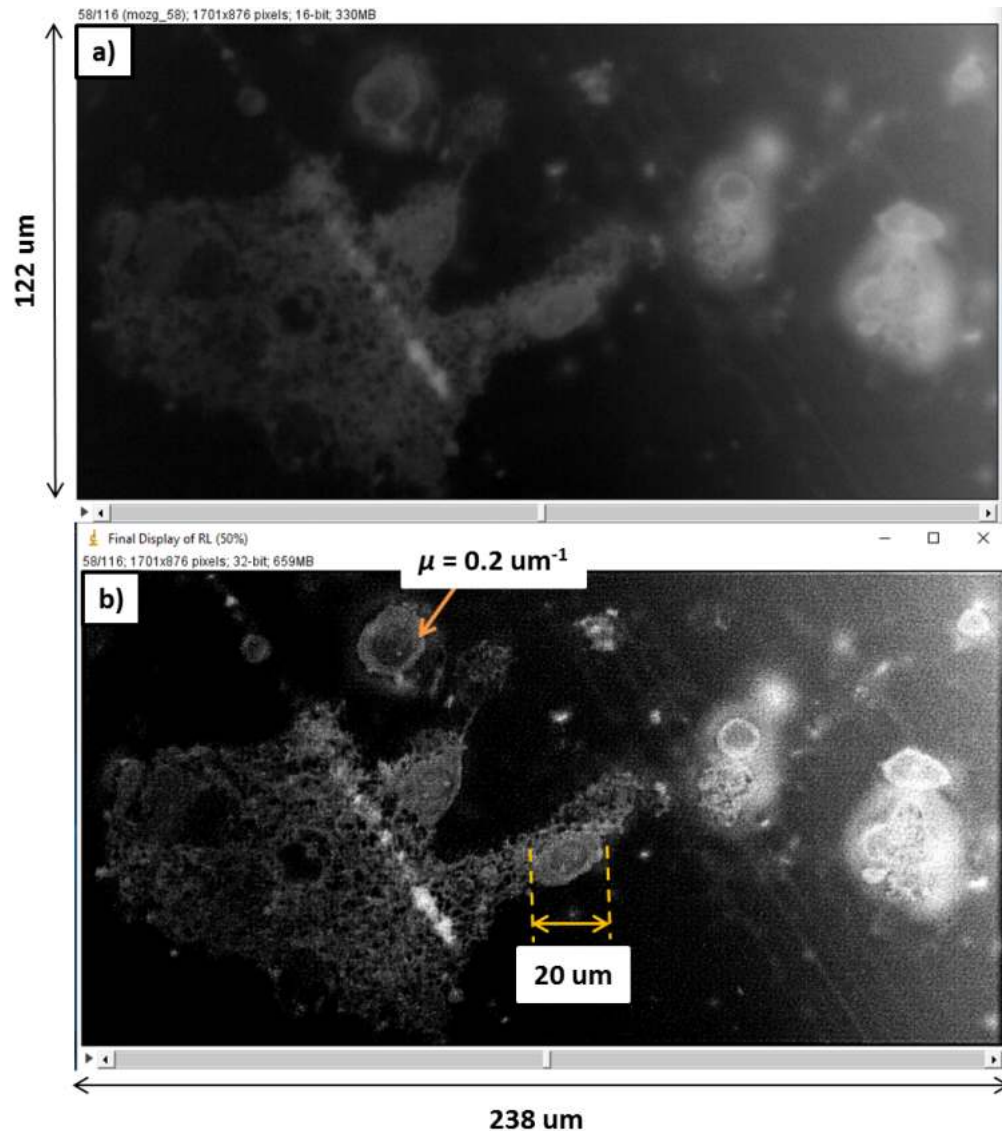


Fig. 14. Focal z-plane of primary cells of mouse hippocampus, obtained on the EUV microscope: a) original image, b) after logarithm and deconvolution by the Richardson-Lucy method with 200 iterations.

5. Conclusion

A full-field, mirror, laboratory EUV microscope working at 13.84 nm has been developed. The methods of ion aspherization and shape correction in combination with point diffraction interferometry made it possible to manufacture an X-ray objective with aberrations at the level of $\text{RMS} = 2.6 \text{ nm}$. Due to the use of a mirror projection lens with a large numerical aperture $\text{NA} = 0.27$ and a short depth of focus, it has been possible, for the first time, to carry out z-tomography of bio-samples with this type of microscope. Its 3D image was reconstructed, with a pixel resolution of 140 nm laterally (corresponding intensity levels are 20–80%). A simple algorithm for the 3D reconstruction of absorption images from z-tomography data formed

in high-aperture soft X-ray microscopes is proposed, which mathematically transforms the absorption inverse problem of finding the absorption coefficient μ to the well-known inverse problem of confocal fluorescence microscopy, for which there are many iterative methods for its solution. Its applicability in the “water transparency window” has been numerically demonstrated. For cells 10 μm thick, the accuracy of the method is about 10%. The advantage of the proposed method is taking into account an experimentally measured PSF of a microscope. The method was used to reconstruct images of bio-samples (dried sections of lily of the valley and mouse primary hippocampal cells) obtained using the microscope developed. Due to the relatively short depth of focus, an axial resolution of 0.42 μm ($\approx 2\text{DOF}$) was obtained (intensity levels are 20–80%). Further improvement will involve increasing the magnification of the EUV microscope to $350\times$ by introducing an additional convex mirror, which will reduce the pixel projection to 18 nm. In the EUV range, the penetration depth into water and into protein is almost the same, so living samples cannot be seen. For this reason, we also plan a modernization of the microscope in the “water window”. In this range, due to the 10 - 15 fold contrast between water and protein, it will be possible to observe non dried cells. Also, a high aperture will allow us to sharply see the focal section, and therefore observe its dynamics in living cells.

Funding. Russian Science Foundation (22-62-00068).

Disclosures. The authors declare no conflicts of interest.

Data availability. Data underlying the results presented in this paper are not publicly available at this time but may be obtained from the authors upon reasonable request.

References

1. E. Hanssen, C. Knoechel, M. Dearnley, M. Dixon, M. Le Gros, C. Larabell, and L. Tilley, “Soft X-ray microscopy analysis of cell volume and hemoglobin content in erythrocytes infected with asexual and sexual stages of *Plasmodium falciparum*,” *J. Struct. Biol.* **177**(2), 224–232 (2012).
2. D. Sage, L. Donati, F. Soulez, D. Fortun, G. Schmit, A. Seitz, R. Guiet, C. Vonesch, and M. Unser, “DeconvolutionLab2: An open-source software for deconvolution microscopy,” *Methods* **115**, 28–41 (2017).
3. G. Vicidomini, P. Bianchini, and A. Diaspro, “STED super-resolved microscopy,” *Nat. Methods* **15**(3), 173–182 (2018).
4. V. Lučić, A. Rigort, and W. Baumeister, “Cryo-electron tomography: The challenge of doing structural biology in situ,” *J. Cell Biol. Review* **202**(3), 407–419 (2013).
5. K.E. Leigh, P.P. Navarro, S. Scaramuzza, W. Chen, Y. Zhang, D. Castaño-Díez, and M. Kudryashev, “Subtomogram averaging from cryo-electron tomograms,” *Methods Cell Biol.* **152**, 217–259 (2019).
6. P. A. C. Takman, H. Stollberg, G. A. Johansson, A. Holmberg, M. Lindblom, and H. M. Hertz, “High-resolution compact X-ray microscopy,” *J. Microsc.* **226**(2), 175–181 (2007).
7. C. A. Larabell and M. A. Le Gros, “X-ray Tomography Generates 3-D Reconstructions of the Yeast, *Saccharomyces cerevisiae*, at 60-nm Resolution,” *Molec. Biol. Cell* **15**, 957–962 (2004).
8. D. Weib, G. Schneider, B. Niemann, P. Guttmann, D. Rudolph, and G. Schmah, “Computed tomography of cryogenic biological specimens based on X-ray microscopic images,” *Ultramicrosc.* **84**(3-4), 185–197 (2000).
9. M. Bertilson, O. von Hofsten, U. V.A. Holmberg, E. A. Christakou, and H. M. Hertz, “Laboratory soft-x-ray microscope for cryotomography of biological specimens,” *Opt. Lett.* **36**(14), 2728–2730 (2011).
10. M. Bertilson, O. von Hofsten, U. Vogt, A. Holmberg, and H.M. Hertz, “High-resolution computed tomography with a compact soft x-ray microscope,” *Opt. Express* **17**(13), 11057–11065 (2009).
11. M. Toyoda, K. Yamasoe, T. Hatano, M. Yanagihara, A. Tokimasa, T. Harada, T. Watanabe, and H. Kinoshita, “At-wavelength extreme ultraviolet lithography mask observation using a high-magnification objective with three multilayer mirrors,” *Appl. Phys. Express* **5**(11), 112501 (2012).
12. L. Juschkin, R. Freiberger, and K. Bergmann, “EUV microscopy for defect inspection by dark-field mapping and zone plate zooming,” *J. Phys.: Conf. Ser.* **186**, 012030 (2009).
13. A. Torrisi, P. Wachulak, L. Wegrzynski, T. Fok, A. Bartnik, T. Parkman, S. Vondrova, J. Turnova, B.J. Jankiewicz, B. Bartoszewicz, and H. Fiedorowicz, “A stand-alone compact EUV microscope based on gas-puff target source,” *J. Microsc.* **265**(2), 251–260 (2017).
14. P. W. Wachulak, A. Torrisi, A. Bartnik, L. Wegrzynski, T. Fok, and H. Fiedorowicz, “A desktop extreme ultraviolet microscope based on a compact laser-plasma light source,” *Appl. Phys. B* **123**(1), 25 (2017).
15. T. Ejima, F. Ishida, H. Murata, M. Toyoda, T. Harada, T. Tsuru, T. Hatano, M. Yanagihara, M. Yamamoto, and H. Mizutani, “High throughput and wide field of view EUV microscope for blur-free one-shot imaging of living organisms,” *Opt. Express* **18**(7), 7203–7209 (2010).
16. W. Chao, P. Fischer, T. Tyliczszak, S. Rekawa, E. Anderson, and P. Naulleau, “Real space soft x-ray imaging at 10 nm spatial resolution,” *Opt. Express* **20**(9), 9777–9783 (2012).

17. V. De Andrade, V. Nikitin, M. Wojcik, A. Deriy, S. Bean, D. Shu, T. Mooney, K. Peterson, P. Kc, K. Li, S. Ali, K. Fezzaa, D. Gursoy, C. Arico, S. Ouendi, D. Troadec, P. Simon, F. De Carlo, and C. Lethien, "Fast X-ray Nanotomography with Sub-10 nm Resolution as a Powerful Imaging Tool for Nanotechnology and Energy Storage Applications," *Adv. Mater.* **33**(21), 2008653 (2021).
18. I.V. Malyshev and N. I. Chkhalo, "A method of z-tomography using high-aperture soft X-ray microscopy," *Ultramicroscopy* **202**, 76–86 (2019).
19. <https://www.euvlitho.com/2018/P22.pdf>
20. A. D. Akhsakhalyan, E. B. Kluev, A. Ya. Lopatin, V. I. Luchin, A. N. Nechay, A. E. Pestov, V. N. Polkovnikov, N. N. Salashchenko, M. V. Svechnikov, M. N. Toropov, N. N. Tsybin, and N. I. Chkhalo, "Current Status and Development Prospects for Multilayer X-ray Optics at the Institute for Physics of Microstructures, Russian Academy of Sciences," *J. Synch. Investig.* **11**(1), 1–19 (2017).
21. N. I. Chkhalo, I. V. Malyshev, A. E. Pestov, V. N. Polkovnikov, N. N. Salashchenko, M. N. Toropov, and A. A. Soloviev, "Problems in the application of a null lens for precise measurements of aspheric mirrors," *Appl. Opt.* **55**(3), 619–625 (2016).
22. N.I. Chkhalo, I.V. Malyshev, A.E. Pestov, V.N. Polkovnikov, N.N. Salashchenko, and M.N. Toropov, "Diffraction limited X-ray optics: technology, metrology, applications," *Usp. Fiz. Nauk* **190**(01), 74–91 (2020).
23. Š. Salacová, P. Wachulak, M. Tatfcek, and M. Vrbová, "Gas-puff target for laser-producing plasma SXR source," *Acta Polytech.* **59**(6), 587–592 (2019).
24. I. V. Malyshev, A. E. Pestov, V.N. Polkovnikov, N. N. Salashchenko, M. N. Toropov, and N. I. Chkhalo, "Current State of Development of a Microscope Operating at a Wavelength of 3.37 nm at the Institute of Physics of Microstructures of the Russian Academy of Sciences," *J. Synch. Investig.* **12**(6), 1253–1263 (2018).
25. N.I. Chkhalo, M.N. Drozdov, E.B. Kluev, S.V. Kuzin, A.Ya. Lopatin, V.I. Luchin, N.N. Salashchenko, N.N. Tsybin, and S.Yu. Zuev, "Thin film multilayer filters for solar EUV telescopes," *Appl. Opt.* **55**(17), 4683–4690 (2016).
26. N. I. Chkhalo, A. E. Pestov, N. N. Salashchenko, A. V. Sherbakov, E. V. Skorokhodov, and M. V. Svechnikov, "Sub-micrometer resolution proximity X-ray microscope with digital image registration," *Rev. Sci. Instrum.* **86**(6), 063701 (2015).
27. N. I. Chkhalo, A. Y. Klimov, V. V. Rogov, N. N. Salashchenko, and M. N. Toropov, "A source of a reference spherical wave based on a single mode optical fiber with a narrowed exit aperture," *Rev. Sci. Instrum.* **79**(3), 033107 (2008).
28. <https://www.gpixel.com/products/area-scan-en/gsense/gsense2020bsi/>
29. N.I. Chkhalo, I.A. Kaskov, I.V. Malyshev, M.S. Mikhaylenko, A.E. Pestov, V.N. Polkovnikov, N.N. Salashchenko, M.N. Toropov, and I.G. Zabrodin, "High-performance facility and techniques for high-precision machining of optical components by ion beams," *Precis. Eng.* **48**, 338–346 (2017).
30. A.A. Akhsakhalyan, N.I. Chkhalo, N. Kumar, I.V. Malyshev, A.E. Pestov, N.N. Salashchenko, M.N. Toropov, B.A. Ulasevich, and S.V. Kuzin, "Compact high-aperture interferometer with a diffractive reference wave for high-precision referenceless aberration measurements of optical elements and systems," *Precis. Eng.* **72**, 330–339 (2021).
31. S. Inoué, "Foundations of confocal scanned imaging in light microscopy. Handbook of biological confocal microscopy," Springer, pp. 1–19 (2006).
32. M. Born and E. Wolf, "Principles of Optics: Electromagnetic Theory of Propagation," *Interference and Diffraction of Light*, 595–597 (Cambridge University Press, New York, 1999).
33. M. Uchida, Y. Sun, G. McDermott, C. Knoechel, M. A. Le Gros, D. Parkinson, D. G. Drubin, and C. A. Larabell, "Quantitative analysis of yeast internal architecture using soft X-ray tomography," *Yeast* **28**(3), 227–236 (2011).
34. G. McDermott, M. A. Le Gros, C. G. Knoechel, M. Uchida, and C. A. Larabell, "Soft X-ray tomography and cryogenic light microscopy: the cool combination in cellular imaging," *Imaging Cell Biol. Rev. Spec. Issue.* **19**(11), 587–595 (2009).
35. T.D. Visser, F.C.A. Groen, and G.J. Brakenhoff, "Absorption and scattering correction in fluorescence confocal microscopy," *J. Microsc.* **163**(2), 189–200 (1991).
36. Y.G. Guan, Y.Y. Cai, X. Zhang, Y.T. Lee, and M. Opas, "Adaptive Correction Technique for 3D Reconstruction of Fluorescence Microscopy Images," *Microsc. Res. Tech.* **71**(2), 146–157 (2008).